Acquiring spatially varying appearance of printed holographic surfaces

ANTOINE TOISOUL*, Imperial College London
DALJIT SINGH DHILLON*, Imperial College London
ABHIJEET GHOSH, Imperial College London

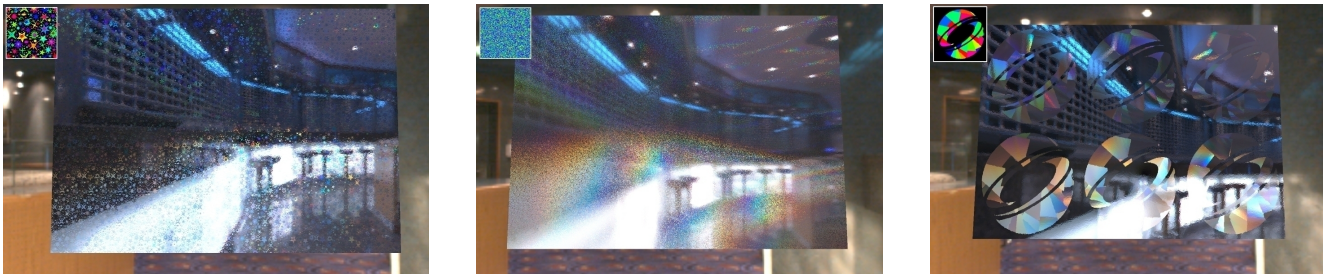

(a) (b) (c)

Fig. 1. Acquired holographic surfaces rendered in real-time under environmental illumination. **(a)** Holographic paper with a repeating star pattern acquired using flash illumination. **(b)** Holographic paper with a stochastic texture acquired using flash illumination. **(c)** A holographic SIGGRAPH logo from a SIGGRAPH 2015 registration badge acquired using polarization imaging. Insets show HSV color visualization of the estimated grating orientation maps.

We present two novel and complimentary approaches to measure diffraction effects in commonly found planar spatially varying holographic surfaces. Such surfaces are increasingly found in various decorative materials such as gift bags, holographic papers, clothing and security holograms, and produce impressive visual effects that have not been previously acquired for realistic rendering. Such holographic surfaces are usually manufactured with one dimensional diffraction gratings that are varying in periodicity and orientation over an entire sample in order to produce a wide range of diffraction effects such as gradients and kinematic (rotational) effects. Our proposed methods estimate these two parameters and allow an accurate reproduction of these effects in real-time. The first method simply uses a point light source to recover both the grating periodicity and orientation in the case of regular and stochastic textures. Under the assumption that the sample is made of the same repeated diffractive tile, good results can be obtained using just one to five photographs on a wide range of samples. The second method is based on polarization imaging and enables an independent high resolution measurement of the grating orientation and relative periodicity at each surface point. The method requires a minimum of four photographs for accurate results, does not assume repetition of an exemplar tile, and can even reveal minor fabrication defects. We present point light source renderings with both approaches that qualitatively match photographs, as well as real-time renderings under complex environmental illumination.

Additional Key Words and Phrases: Diffraction, wave optics, spectral, polarization, real-time rendering.

*Joint first authors.

Authors' addresses: Antoine Toisoul, Department of Computing, Imperial College London, ast13@imperial.ac.uk; Daljit Singh Dhillon, Department of Computing, Imperial College London, djdhillon@gmail.com; Abhijeet Ghosh, Department of Computing, Imperial College London, abhijeet.ghosh@imperial.ac.uk.

1 INTRODUCTION

Measurement based reflectance modeling has been an active area of research for many years in computer graphics. Much of previous work has focused on reflectance that can be modeled with geometric optics including measurement of isotropic [Matusik et al. 2003] and anisotropic [Ngan et al. 2005; Ward 1992] surfaces, and fitting such measurements to appropriate parametric models [Cook and Torrance 1982; Ward 1992]. However, impressive visual effects related to the wave behaviour of light remain challenging from a measurement and rendering point of view. This is the case of diffraction of light, which produces rainbow patterns on surfaces due to the dispersion of white light. Such effects are hard to deal with both in rendering and measurement due to the requirement of complex Fourier optics simulations and the fact that they are caused by surface variations at the micrometer scale. Indeed, diffraction of light only appears when the microgeometry of a surface reaches a size below the coherence length of white light ($65\mu m$ for sunlight [Mashaal et al. 2012]), making measurements hard to carry out without specialized equipment.

Stam [1999] was the first to introduce a Bidirectional Reflectance Distribution Function (BRDF) for diffraction based on Kirchoff theory. His BRDF is computed from a height field that describes the variations of a surface at the microscopic scale. Although it can theoretically be used to render any type of non volumetric diffraction, the BRDF is very expensive to compute and obtaining a height field to produce a specific type of diffraction is not straightforward. Dhillon et al. [2014] solved this problem and presented photorealistic renderings of diffraction in biological structures using height fields that were measured with an Atomic Force Microscope. Although very accurate, their method requires specialized equipment that is not widely available. Besides, it still requires Fourier computations and is not suitable for real-time rendering under arbitrary environmental illumination. Recently, Toisoul and Ghosh [2017a] have

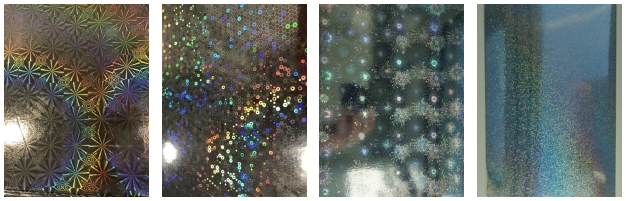

(a) (b) (c) (d)

Fig. 2. Holographic surfaces with different diffraction effects. **(a)** Book cover with kinematic rotation effect. **(b)** Gift bag with circular diffractive areas. **(c)** Holographic paper with firework effect. **(d)** Stochastic texture that produces iridescent glitter. a, c and d are A4 in size.

presented an image-based technique that is practical for computer graphics applications based on direct measurement of diffraction patterns created on homogeneous samples using spectrally filtered flash illumination. Besides assuming a homogeneous sample, the technique additionally requires the diffractive sample to be large enough to observe the entire pattern from a single viewpoint. These two assumptions do not hold for many diffractive objects, and in particular for holographic surfaces. Such surfaces are often made of textures with tiny features, each of which having a different diffraction pattern that needs to be measured without being able to observe the pattern entirely (see Fig. 2 for few such surfaces).

In this work, we focus on specific type of planar spatially varying holographic surfaces that are cheaply manufactured using one dimensional diffraction gratings that diffract light in specific directions depending on their orientation and at specific angles depending on their periodicity (see Section 1 in supplemental material). Although this may seem to be a strong simplification, such holographic surfaces are very common (e.g., gift bags, holographic papers, security holograms) and are able to produce a wide range of impressive well known optical effects such as kinematic, gradient and firework like effects (see Fig. 2).

Originally, orientation and periodicity maps for these surfaces are custom designed and the gratings are printed accordingly. However, such data is not readily available for computer graphics and reverse engineering the orientation and periodicity from simple observations is rather difficult, especially under natural lighting. We propose two novel approaches to measure orientation and periodicity maps of such surfaces and demonstrate how the data can be used to qualitatively reproduce these effects in rendering. We also provide datasets of measured spatially varying orientation and periodicity maps and demonstrate how these maps can be modified to create new visual effects.

In summary, our contributions are as follows :

- We present a practical method to measure spatially varying grating orientations and periodicities using a few photographs taken with flash illumination. The technique works best with planar holographic surfaces that are made of repeating tiles and have a set of discretized orientations and periodicities, as well as holographic surfaces with stochastic gratings.
- We present a complimentary method based on polarization imaging that recovers independent grating orientations and relative periodicities per surface point which is suitable for holographic surfaces with non repeating grating variations (both discrete and continuous). To our knowledge, this is the first wave optical setup that measures anisotropy due to surface structures at wave optics scale.
- We provide high resolution datasets of measured spatially varying orientation and periodicity maps for common holographic surfaces. These can be employed to combine and create new effects as well as help understand how to design maps in order to achieve a specific target effect.

2 RELATED WORK

In the following, we discuss the most relevant previous work on diffraction effects in surface reflectance, as well as other wave effects including polarization.

2.1 Diffraction effects

Stam [1999] first introduced a general model for diffraction based on Kirchoff theory. His model is an extension of the He-Torrance model [He et al. 1991] to include anisotropy and requires as an input a height field h that describes the microscopic variations of height of the diffraction grating. The diffraction contribution in the BRDF comes from a p function that is dependent on both the height-field h and the viewing and incoming light directions and has to be calculated at every frame of an animation. As a result, the general form of the BRDF cannot be computed at real-time framerates since it requires the computation of a two-dimensional Fourier transform of the correlation of the p function.

Sun et al. [2000] rendered iridescence in optical discs by modelling the grooves on a CD as consecutive spheres. Although their method produces realistic results of iridescence on optical disks, the approach is specific to CDs. Agu and Hill [2002] derived an analytic diffraction model based on the Huygens-Fresnel principle for multislit diffraction along one dimension, i.e., diffraction produced by a periodic microstructure made of rectangles. Instead, in this work we model each dot on a holographic surface as a 1-D sinusoidal grating and derive its formulation from Stam's BRDF. Lindsay and Agu [2006] have proposed adaptively sampling the diffractive BRDF into spherical harmonics (SH) basis for real-time rendering. However, the reconstructed diffraction pattern does not preserve high frequencies due to usage of low order SH basis for lighting and BRDF. Cuypers et al. [2012] have instead proposed a very general diffraction wave BSDF using Wigner distributions that supports both direct and multiple bounce simulations of diffraction using a ray-tracing framework. Similar to Stam, this approach requires the underlying microstructure of the grating as input.

Dhillon et al. [2014] recently proposed a reformulation of Stam's BRDF using a Taylor expansion to break the dependency between the height field and the viewing and incoming light direction. This allows a precomputation of diffraction look up tables (terms of the Taylor expansion) using windowed Fourier transforms that can be employed for real-time rendering. They also proposed a measurement approach to record diffraction microstructures of biological specimens (snake skin) using a specialized Atomic Force Microscope

(AFM). Subsequently, Dhillon and Ghosh [2016] have proposed employing Chebyshev polynomials to compress the large number of terms of Taylor expansion required by [Dhillon et al. 2014] (usually 30 – 80), and demonstrated good qualitative results using a second order polynomial.

Kang et al. [2015] have instead proposed an RGB diffraction model that avoids full spectrum computations and evaluates a microfacet BRDF model at different rotations of the half-vector for each color channel, producing a separation of colours. Although very simple to implement, their model does not guarantee physically correct rendering. For measurements of microstructure, Dong et al. [2015] have proposed employing a profilometer to measure the microstructure of metallic surfaces and drive both a microfacet BRDF as well as a Kirchhoff scattering based BRDF model for rendering the aggregate surface appearance. Although the microgeometry measurements with a profilometer are down to the scale of the wavelength of visible light, diffraction effects were not modeled in this work.

Holzschuch and Pacanowski [2017] have recently proposed a two scale modeling of surface reflectance, driving microstructure larger than the wavelength of visible light with standard microfacet model while modeling diffraction within smaller microstructure approaching wave optics scale. They demonstrate that this dual scale BRDF modeling better fits measured data. Werner et al. [2017] have instead proposed a technique for modeling and rendering iridescent diffraction in spatially resolved scratches using non-paraxial scalar diffraction theory. Surface scratches as modeled as collection of line segments and individual diffraction patterns of contributing segments within a footprint are analytically computed and superimposed. The approach has recently also been extended for real-time rendering including closed-form solutions for modeling spherical and polygonal area light sources [Velinov et al. 2018]. Yan et al. [2018] have recently further generalized the approach for rendering subtle colored glints due to arbitrary surface microstructure. However, these recent works do not model strong iridescent effects due to diffraction in manufactured materials.

Closest to our work, Toisoul and Ghosh [2017a] have proposed direct image-based measurement of strong diffraction patterns observed on homogeneous samples and drive a data-driven diffraction BRDF model for real-time rendering. They also demonstrate view-dependent rendering under complex environmental lighting using pre-filtering. In subsequent work, Toisoul and Ghosh [2017b] employ low rank factorization of acquired 2-D diffraction patterns for efficient real-time rendering. We employ their rendering method in this work for rendering spatially varying 1-D sinusoidal gratings under complex environmental illumination.

2.2 Other wave effects

Researchers have investigated other iridescent effects in surface reflectance. Sun et al. [2000; 1999a; 1999b] have extensively studied full spectral rendering for modeling iridescence due to thin film interference. In subsequent work, Sun [2006] proposed an RGB-based renderer for efficient simulation of biological iridescence. Granier and Heidrich [2003] have also proposed a simplified RGB-based BRDF model for modeling iridescence in layered materials. Imura et al. [2009] have proposed rendering structural colors in reflectance due to thin film or multi-layer interference as well as diffraction in a unified framework of optical path differences in microstructure. Belcour and Barla [2017] have recently proposed an extension for microfacet BRDFs based on analytic spectral integration to accurately model thin film interference due to varying thin film thickness over a rough surface. Also related is the work of Hullin et al. [2010] who employed spectral BRDF measurements for modeling bispectral materials exhibiting fluorescence.

Wave effects have also been considered by Levin et al. [2013] for fabricating BRDFs with high spatial resolution, and by Ye et al. [2014] for creating custom BxDF displays based on multilayer diffraction. These works aim at fabricating structures that match given reflectance characteristic, whereas in this work we measure spatially varying grating parameters to reproduce diffraction effects in common holographic surfaces.

2.3 Polarization modeling and imaging

Polarization effects in surface reflectance have recently received some attention in computer graphics, both for rendering as well as inference. Weidlich and Wilkie [2008] studied polarized light transport in uniaxial brifringent crystals and proposed appropriate ray tracing with Mueller calculus for modeling the characteristic double transmission through such crystals due to ordinary and extraordinary rays. Berger et al. [2012] have employed ellispometry to validate polarized surface reflectance in various metals against predictions of microfacet models.

Closest to our work, Ghosh et al. [2010] have proposed measurement of the full Stokes parameters of polarized reflectance under circularly polarized incident illumination to estimate a complete set of parameters for an isotropic BRDF, including index of refraction. Similarly, Riviere et al. [2017] have recently employed linear polarization imaging for surface reflectometry under uncontrolled outdoor illumination exhibiting partial linear polarization. Our polarization imaging setup is inspired by these works. However, due to practical considerations, we employ a combination of circularly polarized illumination and linear polarization imaging in this work for estimating spatially varying anisotropic grating parameters in manufactured holographic samples. Furthermore, instead of Mueller calculus, we employ the reduced Jones calculus for our analysis.

3 OVERVIEW

Figure 3 depicts the structural aspects of dot-matrix holographic prints. We refer the interested reader to the supplemental material for a brief background on the manufacturing process of common holographic surfaces. The rest of the paper is organized as follows: we present a simple measurement setup employing flash illumination in Section 4 to acquire spatially varying orientations and periodicities of planar holographic surfaces made up of a repetitive exemplar tile containing a discrete set of orientations. The method is also suitable for surfaces with stochastic variation of grating orientations and periodicities. We present a more complex setup based on polarization imaging in Section 5 that resolves truly spatially varying non-repeating grating structures with continuous orientations. Section 6 presents additional results including real-time environmental renderings and examples of editing the maps for

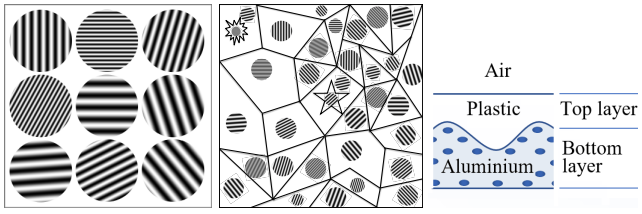

(a) Grating dots (b) Surface layout (c) Grating cross-section

Fig. 3. Illustration of grating dot matrix prints in a holographic film/paper. **(a)** A close-up of hot-pressed grating dots on a plastic material. Grayscale represents local depth variations from white as the top and black as the bottom level. **(b)** The grating dots are organized in a specific layout that makes a spatially varying holographic surface. **(c)** A cross-section on a holographic dot showing sinusoidal grating structure on a metal base layer with a protective plastic top layer.

creating new visual effects. Finally, Section 7 presents evaluations of the two proposed methods.

4 ACQUIRING REPETITIVE SAMPLES

We first describe a very simple procedure to recover the grating orientations and periodicities of planar spatially varying holographic surfaces consisting of a repeating master tile. The method only requires a small set of photographs of a sample under point source illumination, resulting in a very accessible measurement process. We further describe in Section 4.5 how the same measurement setup can also be used to recreate iridescent effect from stochastic holographic surfaces by sampling the joint probability distribution of the orientations and periodicities.

4.1 Flash illumination measurement

The acquisition setup only requires a point light source for which we employ an iPhone 5S smartphone flash, and a camera for which we employ a Canon 750D DSLR (Fig. 4a). During acquisition, we illuminate the sample with the flash and record the resulting diffraction pattern on the sample. The distance between the camera and the sample is chosen such that the entire sample can be observed while having the highest resolution possible for each repeating tile (about 50 centimeters in our case). The distance between the light source and the sample is chosen such that the entire diffraction pattern is visible. In our experiments, the distance varied between 10 to 30 centimeters. Fig. 4a shows an example of a circular diffraction pattern observed on a holographic paper made of a repeating tile of polygons. Note that the central specular highlight must be visible in the photograph as its position is later employed to recover both the grating orientations and periodicities.

We generally record several high-dynamic range (HDR) images [Debevec and Malik 1997] of the diffraction pattern for different light positions with a fixed camera. The goal is to obtain a set of photographs in which all the diffractive areas of the sample diffract light in at least one of the photographs. If the holographic surface is made of a repeating tile, it will only be necessary to solve for a smaller region that corresponds to a master exemplar tile. As a result, fewer photographs are required as several unique observations of the same tile can be obtained over the entire sample. In our experiments, one to five photographs were required to recover the exemplar tile depending on the complexity of the pattern drawn on the holographic sample and the number of times the tile is repeated. This varied from 6×4 repetitions to 10×8 repeated tiles depending on the sample we acquired. Finally, we also take a photograph under house light illumination in order to be able to clearly see and select the repeating tiles on the holographic surface (see Fig. 4b). Note that Aittala et al. [2015] have previously employed similar flash illumination to measure SVBRDF parameters of stochastic textures but their work focused on geometric optics.

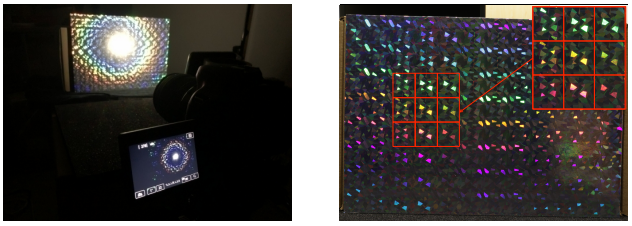

(a) (b)

Fig. 4. **(a)** Measurement setup consisting of a DSLR camera recording the diffraction pattern on a sample due to a phone flash. **(b)** Photograph of the holographic paper under house lights. Note how the polygonal pattern repeats over the sample.

4.2 Sinusoidal grating model

We now derive a BRDF model for the holographic surface under the assumption that it is made of one dimensional sinusoidal diffraction gratings. This assumption allows us to recover spatially varying orientation and periodicity maps for rendering from our measurements. The height field of a sinusoidal grating orientated along the x axis is given in Eq. 1. The parameter a corresponds to the periodicity of the grating, and h_0 its height.

$$h(x,y) = \frac{h_0}{2}(1 + cos(2\pi\frac{x}{a})) \tag{1}$$

For such a height field, we can derive an analytic solution of Stam's BRDF [Stam 1999] assuming a Gaussian coherence window and a second order Taylor expansion [Dhillon et al. 2014]. The full derivation is explained in the accompanying supplemental document. The final formulation of the BRDF has the following form:

$$\begin{aligned} f_r(\omega_i,\omega_o,\lambda) = C(\omega_i,\omega_o)\int_\lambda (&\alpha_0(\lambda,h_0)G^2(\frac{2\pi}{\lambda}(u,v)) \\ +&\alpha_1(\lambda,h_0)G^2(\frac{2\pi}{\lambda}(u-\frac{\lambda}{a}),v) + \alpha_{-1}(\lambda,h_0)G^2(\frac{2\pi}{\lambda}(u+\frac{\lambda}{a}),v) \\ +&\alpha_2(\lambda,h_0)G^2(\frac{2\pi}{\lambda}(u-\frac{2\lambda}{a}),v) \\ +&\alpha_{-2}(\lambda,h_0)G^2(\frac{2\pi}{\lambda}(u+\frac{2\lambda}{a}),v))S_{XYZ}(\lambda)d\lambda \end{aligned} \tag{2}$$

In the (u,v) space, i.e in the space that corresponds to the projection of the non normalized half vector onto the tangent and

bitangent of the diffraction grating, the BRDF is a linear combination of Gaussians centered at $(0, 0)$ for the specular highlight, $(\pm\frac{\lambda}{a}, 0)$ for the first order of diffraction, and $(\pm\frac{2\lambda}{a}, 0)$ for the second order of diffraction. Note that the second order Taylor expansion limits the diffraction to the second order lobes which reduces the computational expense for rendering. Besides, high order diffraction lobes are only visible at grazing angles and quite often far enough from the specular highlight to not be seen on the sample. Note that the one dimensional grating only diffracts light along its main orientation (here the x axis). This formulation of the BRDF allows us to recover both the grating orientations and corresponding periodicities as explained in the following sections.

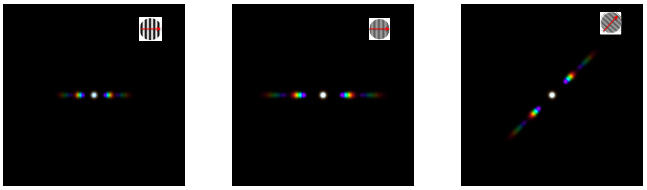

(a) (b) (c)

Fig. 5. Rendering of the diffraction pattern of a sinusoidal grating with varying grating orientation and periodicity under the second order approximation. **(a)** Axis aligned grating with low periodicity of 600 lines per millimeter. **(b)** Axis aligned grating with higher periodicity of 1000 lines per millimeter. **(c)** Sinusoidal grating orientated at 45 degrees with a periodicity of 1000 lines per millimeter. The pattern aligns with the orientation of the grating.

4.3 Grating orientation

As can be seen in the renderings of Fig. 5a one dimensional grating only diffracts light along its main direction. Hence if an order of diffraction is observed at a surface point, the orientation of the grating at that point is given by the orientation that the vector towards the specular highlight makes with the x axis. This direction will be denoted as the tangent to the grating. Note that because the grating is symmetric, the observation of a positive or a negative order of diffraction is not important as the grating direction will remain the same modulo 180° rotation. As a result, inferring the grating orientation from the measured data can be done in several steps. First, a homography correction is applied on the photographs in order to correct any misalignment. This is done by selecting the four corners of the planar samples. Then all the repeating tiles on the sample are manually selected (see Fig. 4b for a sense of the repetition) and we apply homography corrections to align each tile to the same coordinate frame of reference.

The final step is to find the pixels that diffract light in the input photographs. This is done using an intensity threshold on the pixels that are outside the specular region. Note that the intensity is a measurement of the confidence that the grating orientation is correct. The higher the intensity, the closer the estimate of the correct orientation. We employ this confidence measure due to the fact that the flash is not a perfect point light with an infinite coherence window. As a result, the response is not a delta Dirac but a Gaussian lobe as shown in the accompanying supplemental document. In order to take this into account, we first look for pixels with a high intensity threshold and then progressively decrease the threshold until all the orientations in the exemplar tile are computed.

Theoretically, it is sufficient to just observe half of the diffraction pattern on the sample due to the symmetry of sinusoidal gratings (observing positive or negative orders of diffraction give the same orientation). In practice, it is best to observe as many diffracted pixels as possible as it decreases the number of photographs required to recover the complete exemplar tile. The recovered orientation map of the exemplar tile for the polygonal holographic paper seen in Fig. 4 is shown in Fig. 6b. However, the orientations alone are not sufficient to render the holographic surface as the grating periodicity has to also be estimated at each surface point.

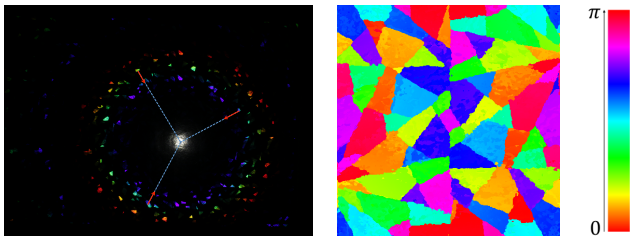

(a) (b) (c)

Fig. 6. Computation of the grating orientations at each surface point. **(a)** The local orientation of the diffraction grating at each diffracted pixel is given by the direction towards the specular highlight (shown by the red vectors). **(b)** Recovered master exemplar tile with angles encoded in HSV space. **(c)** HSV color wheel showing orientations and their corresponding color.

4.4 Grating periodicity

Although some holographic surfaces are made of grating dots that all have the same periodicities, in general such surfaces can have spatially varying periodicities as well as orientations. This can be easily identified on a sample by looking at whether a given color is diffracted at a fixed distance from the specular highlight or at varying distances across the sample (see Fig. 7). In the former case, we only solve for a single periodicity for the entire sample whereas in the latter case we solve for periodicities at each surface point.

In Section 4.2, we showed that the location of a diffraction order for a sinusoidal grating is directly linked to the periodicity of the grating, the diffracted wavelength λ as well as the projection of the non normalized half vector onto the tangent of the grating (variable u). If these two parameters are known, the periodicity of the grating is given by:

$$a = \frac{n\lambda}{|u|} \tag{3}$$

where n is the order of the observed diffraction. A visual explanation of the periodicity variation on the diffraction pattern is shown in Fig. 5.

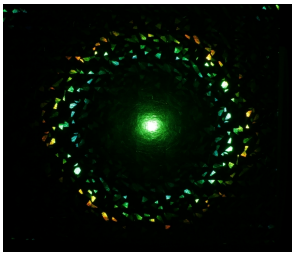

(a) Constant periodicity

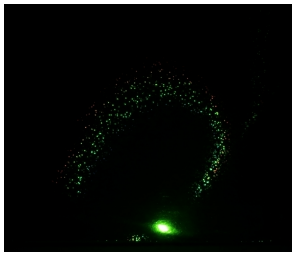

(b) Varying periodicity

Fig. 7. Comparison of two holographic papers illuminated with a spectrally filtered flash. **(a)** Constant periodicity. The green wavelength is diffracted at a fixed distance from the specular highlight, creating a circle. **(b)** Varying periodicity. The green wavelength is diffracted at varying distances from the specular highlight.

In order to measure the periodicity, we attach a green spectral filter (Roscolux thin film sheet with peak at 530 *nm*) in front of the flash during measurements (see Fig. 7) and employ the green channel of the camera in order to spectrally limit the data to a narrow band. Now, estimating the periodicity only requires the computation of the non normalized half vector at each pixel on the sample. Ideally, this requires calibrating the camera and knowing the exact 3D light position. In practice, precise calibration of the camera was not required as the observations are done at normal incidence. As a result, the light directions and view vectors over the entire sample can be approximately calculated if the camera and light distance to the sample are known. We do this in several steps by first applying an homography correction to the entire sample and then finding a correspondence between pixels and real world size. This correspondence is found by neglecting the camera optical distortion and using a known distance on the sample (e.g., the paper is 29.7 centimeter wide in our case). This allows us to compute an approximate distance between the specular highlight and any first order diffracted pixel which gives us the x and y coordinates of the light direction (z is known from the sample-light source distance). The view vector is computed by assuming that the center of the image before homography correction corresponds to the center of the camera. The x and y coordinates of the view vector are then computed by using the distance between the center and a diffracted pixel (the z coordinate is given by the sample-camera distance).

The non normalized half vector can be computed with the above procedure and projected on the grating direction giving us a measurement of u. Finally, the grating periodicity can be estimated using Eq. 3 with $n = 1$ for first order diffraction measurements. We found that with the above approximate calibration procedure, the periodicity can be estimated up to a scaling factor which is sufficient for reproducing the desired visual effect in rendering. If required, explicit camera calibration can instead be employed for increased accuracy of periodicity estimation (see Section 7.1). Having recovered both the orientation and periodicity maps, we can evaluate the BRDF of Eq. 2 in real-time on a modern GPU (e.g., NVIDIA 1080). Fig. 8 shows a point light source rendering of the polygonal holographic surface with the recovered orientations and a single measured periodicity for the entire sample that qualitatively well matches a reference photograph.

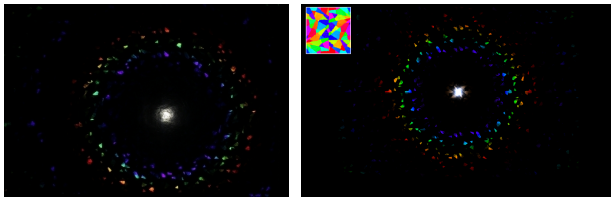

(a) (b)

Fig. 8. Rendering comparison to photograph for polygonal holographic paper. **(a)** Photograph. **(b)** Rendering. Inset shows HSV color visualization of the recovered orientation map.

4.5 Stochastic holographic surfaces

The method described in previous sections work well for recovering the orientations and periodicities of regular non-stochastic holographic surfaces. However, a specific type of holographic surface is made of a stochastic texture that generates a distinct diffraction pattern (e.g., spiral in Fig. 7b). In such samples, the grating dots are printed with a random orientation and periodicity and in such a manner that it creates the desired diffraction pattern at the macro-scale. We model this randomness as being drawn from a joint probability distribution on the orientations and periodicities. We use a spectral filter on the light source and employ the same method described in Sections 4.3 and 4.4 to measure a set of orientations and corresponding periodicities that are found on such a holographic surface. Given the stochastic randomness, we employ a single input photograph for the measurement. The obtained set is an estimation of the true joint probability distribution of orientations and periodicities. Note that the spectral filter is required as different wavelengths can be diffracted by the same set of angles/periodicities giving redundant information and an incorrect estimation of the joint distribution.

The estimated joint distribution can then be used to recreate appropriate tangent and periodicity maps that will generate a similar diffraction pattern in rendering. This is done by stochastically creating a texture from an input shape (e.g disk, square), with each shape having an orientation and periodicity drawn from the estimated joint probability distribution. Fig. 9 shows an example of the rendering of a spiral diffraction pattern created by a stochastic texture made of squares. The joint distribution of orientations and periodicities of the squares is estimated from the corresponding input photograph. As can be seen, the generated maps automatically reproduce a spiral in rendering which qualitatively mimics the photograph. Note that our approach is related to the work of Jacob et al. [2014] on a microfacet BRDF model for the rendering of surfaces with stochastic specular glitter. However, our method goes further to render holographic glints besides specular ones from measurements.

4.6 Limitations

The above described simple acquisition method works with a few photographs under the assumption that the holographic surface is made of repeating tiles and is large enough to cover the specular

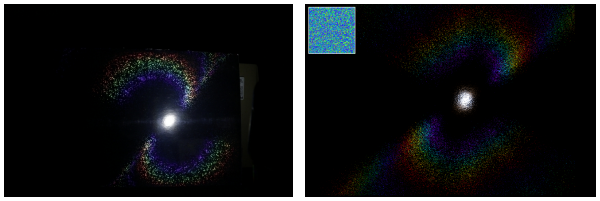

(a) Photograph (b) Rendering

Fig. 9. Comparison of the photograph and rendering of a stochastic paper with varying periodicities. Inset shows HSV color visualization of the grating orientation map.

(a) (b)

Fig. 10. Limitations of flash illumination based acquisition. **(a)** SIGGRAPH 2015 registration badge holographic logo is an example of a small non-repeating sample. **(b)** Kinematic tile with continuous tangent variations is discretized with flash illumination measurements.

lobe and first order diffraction. This is not always the case, as can be seen in the case of the holographic logo on a SIGGRAPH 2015 registration badge (see Fig. 10a). For such samples, recovering the orientations and periodicities is difficult using a point light source due to the sample size as well as its non-repeating structure. Even for larger samples with repetitive tiles, due to the sampling introduced by a small set of flash illumination photographs, tangent fields with continuous variations are discretized in the estimated tangent map. This can be seen for the kinematic tile in Fig. 10b. These inherent limitations of the flash illumination measurement are overcome with a more complex setup employing an area source and polarization imaging as explained in the next section.

5 ACQUIRING NON-REPEATING SAMPLES

We now describe a complementary acquisition method for resolving spatially varying orientations and periodicities in planar holographic samples exhibiting true spatial variation without any repeating texture. Instead of a point source illumination, our second method employs an area source in the form of an LCD panel and further exploits the inherent LCD polarization in conjunction with polarization imaging on the camera to obtain an independent estimate of grating orientation and periodicity at each surface point. Unlike when using flash illumination, our second method can handle continuous variations in grating orientations as well as deal with small samples with fine geometric spatial variations, especially those separating diffractive regions from surrounding non-diffractive regions. We begin by first describing our polarization imaging setup and providing an intuition for such measurements in Section 5.1. We then detail the mathematical basis for our imaging setup by describing formulations for specular reflectance as per Jones calculus in Section 5.2. Thereafter, we present derivations and formulations

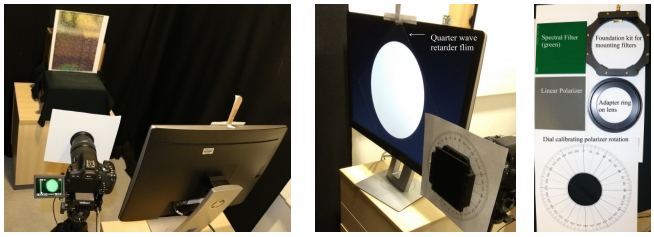

(a) (b) (c)

Fig. 11. Acquisition setup for circularly polarized illumination. (a) Camera and LCD Panel are both positioned fronto-parallel to the sample. (b) A quarter-wave retarder film is mounted at 45° orientation in front of the linearly polarized LCD screen to produce circularly polarized illumination. Camera is mounted with a green spectral filter and a rotatable linear polarizing filter. (c) Optical equipment for filter mounting and rotation.

along with explaining our method details and an example result for the kinematic tile in Section 5.3. Finally, we present the derivations and steps for estimating periodicities on a relative scale in Section 5.4.

5.1 Polarization Imaging Setup

Fig. 11 shows the acquisition setup consisting of an LCD panel (HP EliteDisplay E242) and a DSLR camera (Canon 750D), both positioned near fronto-parallel with respect to the planar sample. The LCD panel is used to simultaneously illuminate an entire diffractive patch on the sample in a single photograph with uniform white illumination. The LCD panel inherently emits linearly polarized illumination which we exploit to image reflected polarization off the sample surface using the camera. We further mount a square sheet of quarter wave retarder (Edmund Optics thin film retarder) at a 45° orientation in front of the LCD panel to convert the linearly polarized illumination into circularly polarized. In order to do this, we limit the uniform illumination pattern on the LCD panel to a circular disc inscribed within the diagonally oriented square retarder sheet. We will explain later in this section why this conversion to circularly polarization is important for the measurements. For imaging the polarization signal, we attach a rotatable linear polarization filter and a fixed green spectral filter in front of the camera lens using a professional filter mounting kit (LEE 100 SYSTEM). The green filter is mounted between the polarizer and the lens and is employed as previously to spectrally isolate the signal around a single wavelength for analysis.

Motivation: For this method to resolve grating orientations from a single non-repeating tile, we need to ensure that each grating dot is lit to reflect light into camera. An obvious choice would be to use an area-light illumination. In past, an LCD panel with appropriate structured lighting patterns has been employed to estimate reflectances with spatial variations due to local surface anisotropies [Tunwattanapong et al. 2013]. To understand the limitations of structured lighting illuminations for our task, consider a tile on a holographic paper with kinematic rotation pattern as shown in Fig. 12a. The tile consists of ten quadrants of continuously rotating grating orientation varying radially from the center, and four smaller such

(a) Response to room lighting

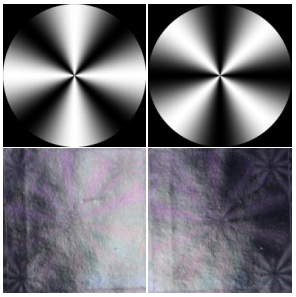

(b) Response to sinusoidal lighting

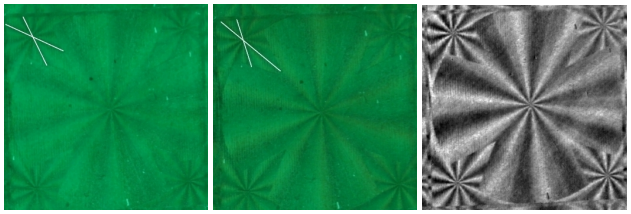

(c) Polarized illumination and imaging

Fig. 12. Holographic paper with kinematic effects. **(a)** Tile viewed under room lighting shows radial bars of different colors and brightness. **(b)** Top row show radially varying sinusoidal patterns that are projected using an LCD panel and bottom row shows the corresponding images of the tile. Pixel brightness in these images is strongly correlated with local surface normal variations and poorly correlated with grating orientations. **(c)** A pair of images acquired with the polarized imaging setup described in Section 5.1. Rotating the linear polarizer filter by 45° turns local minimas of brightness in left image into local maximas in the center image. These changes are illustrated with white line markers for two local minima segments near the top-left corner. Ratio of intensities in two green images is normalized and shown on the right to illustrate relative changes with grating rotation.

centers of radial variations at the tile corners. Fig. 12b shows the kinematic tile's response to two radial sinusoidal patterns emitted by the LCD panel, with the phase of the two sinusoids shifted by a 45° rotation with respect to each other. The sinusoidal patterns are inspired by specific spherical harmonic illumination employed by Tunwattanapong et al. [2013] to estimate local anisotropy. However, unlike surface grooves of brushed metal, the grating anisotropy of the kinematic tile is at a much smaller scale, rendering the sinusoidal lighting patterns ineffective for estimating the local grating orientations. Instead, the sinusoidal patterns can be seen to be responding to the local surface mesostructure (bumps) on the surface of the holographic paper. Instead, when we illuminate the tile with uniform polarized illumination from the LCD panel and take two photographs with a linear polarizer in front of the camera mounted at 0° and 45° orientation (see Fig. 12c), we observe subtle changes in the grating response to the polarizer orientations which can be more clearly seen in the ratio of the two images on the right (grayscale). Clearly, polarized illumination can help resolve grating orientations.

Intuition: Diffraction is essentially a wave optical phenomena which can be influenced by the polarization of incident light wave. Employing polarization imaging can reveal local grating orientations. This is due to relative interference of the incident polarization by the local grating orientation which results in systematic modulation of specular reflections. In fact, we show later how these modulations for each grating dot in our setup can be approximated with a sinusoid that is a function of the rotations for the linearized polarizer filter in front of the camera. The phase offsets for these approximating sinusoids are directly related to the grating orientations of the dots.

Circularly polarized illumination: Our LCD panel emits linearly polarized light with a horizontal orientation. Such linearly polarized lighting itself has a well-defined relation to diffractive reflectances and this relation could in theory be exploited for estimating grating orientations. However, holographic grating samples are commonly manufactured with an additional protective plastic layer which exhibits some birefringence. This causes practical problems of ambiguity in estimating grating orientations when using linearly polarized illumination (please see the supplemental material for details). We overcome this ambiguity in our measurements by transforming the emitted linearly polarized light into circularly polarized illumination using the quarter wave retarder. For acquisition, we still employ linear polarization imaging in conjunction with circularly polarized illumination, and additionally employ a green spectral filter in front of the lens for removing the interference of other spectral bands. Now, for our example in Fig. 12c, the ratios of intensities shows how rotation of the linear polarizer in front of the camera in the proposed setup systematically effects the intensities of reflected light, depending upon gradually varying grating orientations within the kinematic tile. Thus, we image a sample under different rotations of the polarizer filter and employ those images to compute spatially varying grating paramaters through sinusoidal approximations, as explained later. Next, we mathematically describe the effect of various optical elements in our acquisition setup.

5.2 Grating reflectance and Jones calculus

In this section, we formulate the intensity modulation due to specular reflection by an individual grating dot in our acquisition setup. These formulations are used in the next subsection to establish near sinusoidal nature of intensity variations relating to camera polarizer filter rotations. Fig. 13a depicts the imaging schema using a slice along the X-O-Z plane of a global frame of reference. The planar sample is placed at a distance d from the origin with its surface normal pointing towards $-\hat{\mathbf{z}}$. Fig. 13b shows a single holographic dot with local orientation[1] θ in the X-O-Y plane and periodicity p. For simplicity, we assume that the angle of incidence $\phi_i \rightarrow 0$ with near fronto-parallel placements and a baseline $b << d$ between the camera and the LCD screen. We employ Jones calculus to express polarization transformations that a beam of polarized light undergoes while travelling from the LCD panel to the camera. Please refer to Section 3 in the supplemental material for common configurations and transformations of polarized light in Jones calculus. Consider a circularly polarized monochromatic beam with wavelength λ as emitted from its source (LCD panel + wave retarder) in our setup.

[1] θ is negative for the grating dot depicted here as it has a clockwise rotation in the right-handed frame of reference.

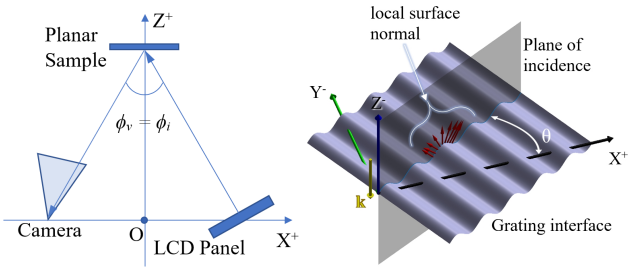

(a) Imaging schema (b) Grating plane of incidence

Fig. 13. Optical geometry for our polarization imaging setup.

This beam is expressed as $\mathcal{E}_i = \mathbf{e_i} \cdot e^{-i(\hat{\mathbf{k}}\cdot\mathbf{x}-\omega t)}$ with $\mathbf{e_i} = (1, -i)^T$ as the Jones vector of complex amplitudes for its polarization and $\hat{\mathbf{k}} = (2\pi/\lambda)\hat{\mathbf{z}}$ as its wave-vector, Here, $\mathbf{x} = d\hat{\mathbf{z}}$ is the position vector for the grating dot under consideration and ω is the temporal angular frequency for light propagation. $\mathcal{E}_i$ is subject to multiple polarization transformations before reaching the camera through ŕeflectance' by the grating dot. The final transformed light wave, say $\mathcal{S}$, can be expressed as

$$\mathcal{S} = \left(r_p \mathbf{F} \times \mathbf{R_f} \times \mathbf{B_R} + t_p \mathbf{S}\right) \times \mathcal{E}_i\,, \quad \mathcal{E}_i = \mathbf{e_i} \cdot e^{i(\hat{\mathbf{k}}\cdot\mathbf{x}-\omega t)}\,, \text{ and} \tag{4}$$

$$\mathbf{S} = \mathbf{F} \times \mathbf{R_f} \times \mathbf{B_T} \times {\mathbf{R_d}}^T \times \mathbf{D} \times \mathbf{R_d} \times \mathbf{B_T} \tag{5}$$

$$= \begin{bmatrix} 1 & 0 \\ 0 & 0 \end{bmatrix} \begin{bmatrix} \cos\psi & \sin\psi \\ -\sin\psi & \cos\psi \end{bmatrix} \begin{bmatrix} 1 & 0 \\ 0 & e^{i\Delta n} \end{bmatrix} \begin{bmatrix} \cos\theta & -\sin\theta \\ \sin\theta & \cos\theta \end{bmatrix} \times \begin{bmatrix} -1 & 0 \\ 0 & R^-/R^+ \end{bmatrix} \begin{bmatrix} \cos\theta & \sin\theta \\ -\sin\theta & \cos\theta \end{bmatrix} \begin{bmatrix} 1 & 0 \\ 0 & e^{i\Delta n} \end{bmatrix}. \tag{6}$$

Eq. 4 represents summation of two waves: (a) a part of the incident wave $\mathcal{E}_i$ which is reflected back from the interface between air and the top plastic layer, and (b) second wave is the rest of $\mathcal{E}_i$ which has undergone transmission through the plastic layer followed by diffraction at the aluminium grating interface and finally transmission out from the plastic layer to air. r_p and t_p represent relative reflectance and transmittance factors for the plastic layer[2]. The first, immediately reflected component of $\mathcal{E}_i$ undergoes a birefringent retardation $\mathbf{B_R}$ due to the plastic layer. This causes it to become slightly elliptically polarized. This partly reflected wave reaches the camera which has a linear polarizer in front of it. Effects of the polarizer filter are mathematically expressed by first rotating the incoming elliptically polarized wave in its local frame of reference through multiplication with the Jones matrix $\mathbf{R_f}$. $\mathbf{R_f}$ represents a rotation of ψ between the linear polarizer filter and the optical axis of the birefringent plastic (assumed to be along X-axis). Finally, the resultant wave is multiplied with matrix $\mathbf{F}$ to express filtered passage through the polarizer filter.

For the second wave component which is transmitted, diffracted back and finally transmitted back into the air[3], its net optical transformation is given by $\mathbf{S}$ which includes following sequence of transformations: (a) First, a birefringent retardation $\mathbf{B_T}$ occurs on transmission through the plastic which converts the wave into elliptically polarized. Without loss of generality, we assume that the optical axis of the birefringent material is aligned with X-axis. If this is not the case, we have to rotate $\mathbf{e_i}$, adding equal phase shifts to both polarizer vectors which can then be ignored in our derivation; (b) This is followed by diffraction. To express reflective diffraction, we first apply a rotation of the transmitted wave into the local frame of reference for the 1D sinusoidal grating by multiplying its Jones vector with matrix $\mathbf{R_D}$. $\mathbf{R_D}$ corresponds to the relative angle θ between the optical axis of birefringence and the grating X-axis. Next, the elliptically polarized light wave gets diffracted from the grating interface according to the transformation $\mathbf{D}$ and travels back with the wave-vector along $-\hat{\mathbf{z}}$. Note that we explicitly include -1 in the top-left of $\mathbf{D}$ to model the 180° relative phase shift upon reflection, which reverses the handedness of the incident wave. Next we bring back the diffracted wave in the original frame of reference by multiplying its Jones vector with ${\mathbf{R_D}}^T$. The diffracted wave experiences same amount of birefringence $\mathbf{B_T}$ on its way out through the plastic layer. The exited wave reaches camera with equal phase shifts in both components of elliptic polarization. These phase-shifts do not change their complex amplitudes or the intensity of reflections and, thus, we ignore them; (c) Finally, as for the first wave component, the second wave component undergoes filtering by the linear polarizer in front of the camera. As before, this filtering transformation is expressed through multiplication with the combined matrix $\mathbf{F} \times \mathbf{R_f}$. The above two wave components superimpose to form the final 'reflected' wave $\mathcal{S}$, as received by the camera. All terms involved in Eq. 4—6 are tabulated in Table 1. Our method works with relative intensities. Thus, all equal scaling or equal phase shifts to complex amplitudes of both polarizer vectors are ignored while deriving above equations. In the following, we describe how Eq. 6 is employed to measure grating orientations with sinusoidal fitting.

Table 1. Symbols and notations.

Notation	Description
$\mathcal{E}_i$	Monochromatic electromagnetic wave incident on a holographic dot
$\mathcal{S}_i$	Electromagnetic wave scattered back to the camera by the dot
r_p,t_p	Scalar coefficients for reflection and transmission with the top-layer plastic material
$\mathbf{B_R}$	Birefringent retardation upon reflection by the top plastic layer
$\mathbf{S}$	Total optical transformation experienced by the wave that get transmitted through the plastic layer, reflected back by the aluminium layer and finally transmitted out of the plastic layer
$\mathbf{B_T}$	Birefringent retardation upon transmission into the plastic layer
$\mathbf{R_d}$	Rotation from the global to the local frame of reference for the grating dot
$\mathbf{D}$	Diffractive transformation
$\mathbf{R_d}$	Rotation from the global to the local frame of reference for the linear polarizer in front of the camera
$\mathbf{F}$	Linearly polarized filtering transformation
$\mathbf{\Delta n}$	Retardation phase difference during transmission in the plastic layer
θ	Clockwise rotation angle between the global and the local frame of reference for the grating dot
R^+, R^-	Complex scale factors for p-polarized and s-polarized wave components in the grating dot's frame of reference
ψ	Clockwise rotation angle between the global and the local frame of reference for the grating dot

5.3 Grating orientation measurement

For plastic materials $r_p \ll t_p$ near normal incidence conditions. Thus for $\mathcal{S}$, its intensity

$$I = \left\|\left(r_p \mathbf{F} \times \mathbf{R_f} \times \mathbf{B_R} + t_p \mathbf{S}\right) \times \mathbf{e_i}\right\|^2 \approx \left\|\mathbf{S} \times \mathbf{e_i}\right\|^2, \tag{7}$$

with $t_p \approx 1$ for our setup. Since our method works with relative intensities, the above approximation is valid even for $t_p \not\approx 1$ as long as it is far greater than r_p and the bottom layer diffracts back nearly

[2]Since we work with near normal incidence conditions, reflectance and transmittance factors are approximately same for both s- and p-polarization.
[3]for simplicity, we assume zero absorption in the plastic layer.

all the light[4]. We now present simplification of Eq. 6, which defines **S** for devising a method to estimate grating orientations.

Case I: No birefringence. Let us consider the simplest case first, i.e. no birefringence. In this case, $\Delta n = 0$ and multiplying $\mathbf{e_i}$ with rotation matrix $\mathbf{R_d}$ only changes the phase of the two components of the circularly polarized incident wave $\mathcal{E}_i$. Thus, without loss of generality, we can set $\theta = 0°$. In this case, $I = \|\mathbf{F} \times \mathbf{R_f} \times \mathbf{D} \times \mathbf{e_i}\|^2$ and it further simplifies to:

$$I = |-(\cos\psi + iR\sin\psi)|^2 \ , \quad \text{where } R = R^-/R^+. \tag{8}$$

In general, R is a complex number and substituting $R = re^{i\zeta}$ in Equation 8 gives us

$$I = 1 + (r^2 - 1)(1 - \cos 2\psi)/2 - r\sin\zeta\sin 2\psi. \tag{9}$$

Setting $\zeta = 0$ gives us our first intuition about sinusoidal profiles for the specular intensity I. In this case, (9) clearly expresses I as a sinusoidal function of ψ which represents the rotations of the linear polarizer filter. Thus, for more general cases, we seek to relate or approximate I as a sinusoidal function of ψ. With this aim, we first normalize I. Let $\bar{I}$ be the mean intensity at a grating dot/pixel for multiple rotations of the linear polarizer filter and I_σ be its scaled standard deviation such that

$$\bar{I} = \frac{1}{\pi}\int_0^\pi I d\psi \quad \text{and} \quad I_\sigma^2 = \frac{2}{\pi}\int_0^\pi (I - \bar{I})^2 d\psi. \tag{10}$$

In this case, the mean $\bar{I} = 1 + (r^2 - 1)/2$ and subtracting it from I gives us $I_0 = I - \bar{I} = -(r^2/2 - 1/2)\cos 2\psi - r\sin\zeta 2\psi$. I_0 is composed of two scaled sinusoids but it does not lend itself to any further analytical simplification. However, we found that for most practical cases, normalizing I as $I_{\text{norm}} = I_0/I_\sigma$ does trace out as a curve that can be well-approximated by a single sinusoidal at twice the frequency of ψ. Thus, we need to devise a way to compute $\bar{I}_r$ and I_σ from images in our polarization setup.

Let the grating dot make an angle θ with our fixed X-axis and let the polarizer filter make an angle ψ_{ref} with the same X-axis. In this case, $\psi = \psi_{\text{ref}} - \theta$. Next, to compute $\bar{I}_r$ and I_σ, we vary ψ_{ref} anticlockwise from 0 to $-\pi$ against X-axis, with N equal step sizes and take corresponding images. We assume that each pixel $\mathbf{x}$ corresponds to a single grating dot and it records a sequence of observed intensities $I^{\mathbf{x}}(\psi_{\text{ref}})$. We use this set to statistically determine its mean $\bar{I}_r^{\mathbf{x}}$ and its standard deviation as $I_\sigma^{\mathbf{x}}$. Using these values we compute $I^{\mathbf{x}}_{\text{norm}}(\psi_{\text{ref}}) = (I^{\mathbf{x}}(\psi_{\text{ref}}) - \bar{I}_r^{\mathbf{x}})/I_\sigma^{\mathbf{x}}$. Next, we fit a cosine function to discretized sample points $I^{\mathbf{x}}_{\text{norm}}(\psi_{\text{ref}})$ with its frequency twice as that for the polarizer filter rotation step. For the best fitting cosine, its phase offset angle η gives the grating orientation $\theta = \eta/2$. Repeat above steps for each pixel in the tile solves for corresponding grating orientations. With simulations to be presented next, we find that the proposed method solves for grating orientations only upto an arbitrary global orientation offset factor. However, this global offset does not impact final renderings subjectively, as demonstrated later.

[4]This is true for our samples with a top-layer of only few micrometers in thickness and the bottom layer is with a metallic coating

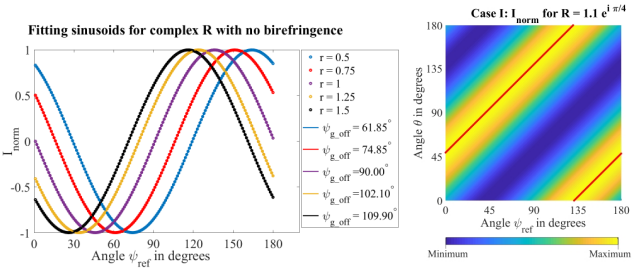

(a) Fitting sinusoids in Case I (b) Specular Intensity I_{norm}

Fig. 14. Simulated specular intensities for different rotations ψ_{ref} of the polarizer filter and grating rotations θ, for cases with no birefringence. (a) shows sine fitting for $0.5 < r < 1.5$, where $R = R^-/R^+ = re^{i\zeta}$. RMS Error for fitting was $\approx 0.002\ \forall r$ shown here. (b) shows specular intensity as a function of ψ_{ref} and θ with indicated color-coding. Red dots overlaid on the intensity map mark respective row maxima and the all fall on a straight line. Thus θ varies linearly with ψ_{ref} when mapped via these maxima.

Simulations for Case I:. We found that sine fitting on $I_{\text{norm}} = I_0/I_\sigma$ works equally well while simulating Equation (9) for a large range of $10^{-4} \le r \le 10^4$. Figure 14a shows simulated values for I_{norm} and corresponding sinusoidal fits when $0.5 < r < 1.5$, $\zeta_{\text{ref}} = \pi/6$ and $\theta = 0$. Similarly, Figure 14b shows maps for relative specular intensities with $r = 1.1$, $\zeta_{\text{ref}} = \pi/4$ and for all values of $\theta = 0$ to π. In this map, we can see that peak intensity values (bright yellow) trace out a linear relation $\theta = \psi + \psi_{\text{g\_off}}$, where $\psi_{\text{g\_off}}$ is a global offset and it varies with R. We tried other values for $\zeta_{\text{ref}} = \pi/3, \pi/2$ and π and the intensity map remains the same as in Figure 14b. Thus, we can use the same method of sinusoidal fitting as in Case I to resolve grating orientations upto an arbitrary global offset $\psi_{\text{g\_off}}$.

Case II: General configuration with birefringence. For samples with birefringence, Eq. 6 cannot be further simplified. Thus, to study the influence of birefringence, we simulated Eq. 6 for different values of birefringence value Δn and the differential diffractive factor $R = R^-/R^+$ in Jones matrix $\mathbf{D}$. For a fixed set of values for R and Δn, we first compute spectral intensity $I = \|\mathbf{F} \times \mathbf{R_f} \times \mathbf{D} \times \mathbf{e_i}\|^2$ for the discretized range of values for θ and ψ_{ref}. Next, for each value of θ, we normalize I to I_{norm}. Fig. 15a shows one such map for the case where the bottom layer is made up of aluminium (complex refractive index: $1.0003 + 6.5044i$ for $\lambda = 560$nm) and the top layer is cellophane (mean refractive index $n = 1.4680$). With these values, we compute $R = R^-/R^+$ for a small angle near $\phi_i = 0°$. For up to $\phi_i = 10°$, the value for R did not change much. We repeated above simulations with six other metals for the base layer (silver, brass, iron, gold, copper and platinum). Intensity maps for these metals are included in the supplemental material. For all these cases and in general, we found that for a birefringence of up to $\Delta n < 10$, there is a near linear relation between ψ_{ref} and θ as highlighted by the dotted line in Fig. 15a. In dot matrix grating manufacturing process using hot embossing, the plastic layer is typically $1\mu m$ thick [Jiang et al. 2014]. Thus, our method can work for materials with birefringent refractive index difference of upto 0.0155. This value covers a large variety of typical birefrengent materials (see [Roff and Scott 2013, Table 60.T1]).

To examine the robustness of our method, we experimented further with hypothetical values for R. We set $R = 1.001 \times \exp(i\zeta)$

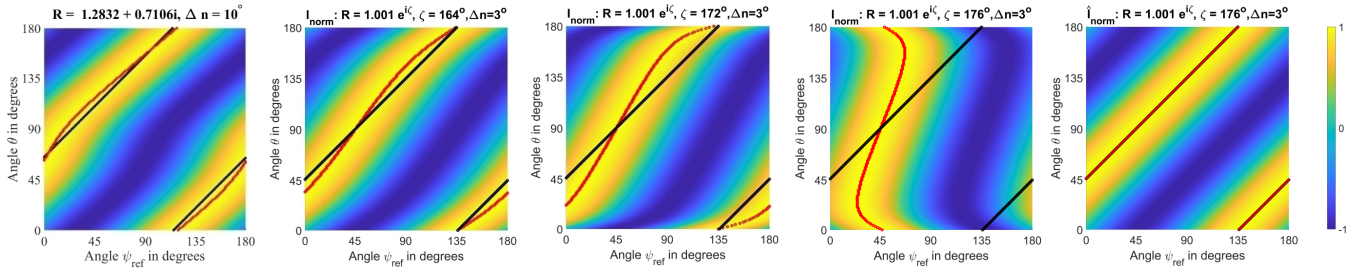

(a) I_{norm} (b) I_{norm} (c) I_{norm} (d) Doubly normalized intensity $\hat{I}_{\text{norm}}$ Vs I_{norm}

Fig. 15. Simulated specular intensity maps for different polarizer filter rotations ψ_{ref} and grating rotations θ. (a)-(d)(left) visualize specular intensity I_{norm} as a color-coded function of ψ_{ref} and θ. All maps correspond to cases with birefringence. (a) corresponds to a practical case of aluminium coated under cellaphone for gratings. (b),(c) and (d) correspond to hypothetical cases of $R = R^-/R^+ = r \exp i\zeta$ which differ only in their ζ values. Red dots indicate a mapping between θ and ψ_{ref} as established through row maxima in each sub-plot. (a) shows that for low grade birefringence of upto 10° we have near linear mapping between ψ_{ref} and θ. Black line in each map indicates expected linear relation in absence of birefringence. For (b) to (d) as ζ increases, the mapping between ψ_{ref} and θ becomes increasingly nonlinear. However, as shown in (d)-right, pre-normalizing images alleviates this issue to produce near linear mappings.

with ζ as a variable while keeping birefringence fixed at $\Delta n = 3°$. Fig. 15b,c and d–(left) show that as ζ varies from 164° to 172° to 176°, the mapping between ψ_{ref} and θ becomes highly non-linear, as established through I_{norm} maxima for each θ. To elevate this issue, we propose a pre-normalization step where we first subtract the mean intensity for all diffractive pixels in an image to first give $\hat{I} = I - \sum_N \frac{I}{N}$ for N diffractive pixels in the image. Next, using $\hat{I}$ in place of I for normalization as present above, we compute $\hat{I}_{\text{norm}} = \frac{\hat{I} - \bar{\hat{I}}}{\hat{I}_\sigma}$. Fig. 15d illustrates the importance of this step with an arbitrary value for R. I_{norm} in the left image shows far from usable mapping between ψ_{ref} and θ with red dots. In this image, each column of the map is considered as an image and used for pre-normalization. Per image normalization rectifies the issue and $\hat{I}_{\text{norm}}$ provides perfectly usable linear mapping between ψ_{ref} and θ as shown in Fig. 15d–(right). In effect, pre-normalization separates and discounts the effects of polarization ellipticity changes due to birefringence from those compounded by diffraction. At the same time, cases with low birefringence are agnostic to it. These facts are verified with qualitative evaluations in Section 6.2 and quantitative evaluations in Section 7.3. Section 5.3 in the supplemental material provides additional details on pre-normalization.

Results. We now demonstrate the working of this method with the kinematic exemplar from Figs. 2 and 12. Kinematic discs show ten-spoked radial pattern of sharp diffracted colors. The spokes rotate as light source moves horizontally or vertically. This subjective effect appears due to continuously varying gradient orientations which are difficult to capture using our flash illumination method. Fig. 16a shows grating orientation map for a single tile using HSV color-coding. We used 13 images taken with linear polarizer rotating by 15° between images to acquire the orientation map. We used MATLAB function *imregister()* to align input images that have offsets due to slight camera movement from manual rotations for the polarizer plate. The exemplar tile is $25mm \times 25mm$ in size. Our grating orientation map has continuous variations from 0 to π in radial directions which are repeated ten times. We measured mean correlation factors for sinusoidal fitting (see Section 7.3). Even with

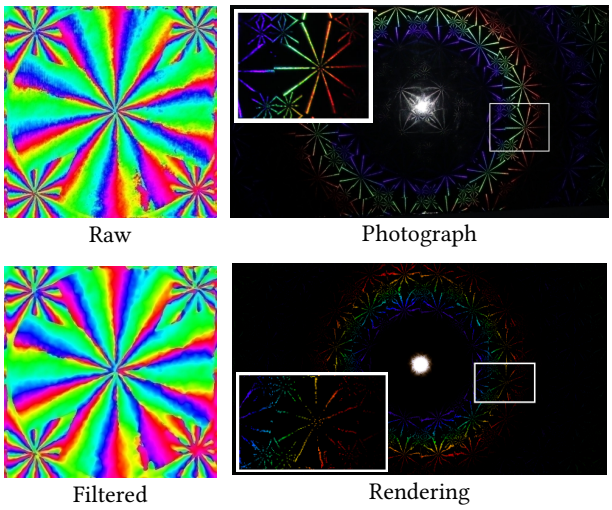

(a) Orientation map (b) Rendering comparison

Fig. 16. Grating orientation map estimated using our polarized acquisition method for a kinematic exemplar tile. 13 images at 15° intervals of filter rotation where used. (a) Raw and bilaterally filtered ($\sigma_{\text{pix}} = 3$, $\sigma_\theta = 0.35$ radians) orientation maps in HSV colors. (b) Rendering with this tile repeated over a plane subjectively matches corresponding photographs. Each inset shows a close-up view of corresponding white box from same image.

high numerical accuracy for this fitting, our method results in a raw map with local variations due to: (a) surface bumps or scratches: they cause local surface normal to violate the near-normal/specular assumption for imaging, (b) grating imperfections: they do not have a valid grating orientation to begin with, (c) overlapping grating dots under single pixel: they violate the assumption about a single grating orientation under pixel, (d) to high a pixel resolution: in this case the observed pixel further modulates the coherence window to cause pixel aperture diffraction effects, and (e) low level of elliptic polarization by the grating: this results in a weak sinusoidal signal that is easily corrupted by noise. We improve imperfections from

these causes by applying an adaptive bilateral filter to the orientation map, as seen in Fig. 16a. We discuss the effects of bilateral filtering on renderings vis-a-vis the use of a raw map, later in Section 6.2 (see Figure 18). Here, Figure 16b shows the rendering of a $20cm \times 30cm$ planar plate with our filtered map repeated all over it's surface. We can subjectively validate that circular bands of colorful spoked-wheels appears around the central highlight in our rendering, just like that for the image above. Also, the key subjective effect of ten bright spokes rotating with light movements is distinctly visible in the accompanying supplemental video. Additional results for the polarization imaging method are presented later in Section 6.2.

5.4 Grating periodicity measurement

The polarization imaging method can also be used to compute grating periodicities on a relative scale. Examining Eq. 6, we can see that only Jones matrix **D** changes with the grating dot's periodicity. Let us study how diffraction efficiency for the zeroth-order diffraction changes with grating periodicity under normal incident illumination. Consider a 1D grating expressed as a height-field $h(x, y)$ with period p for variations only along its X-axis. Under conditions for our imaging setup, the specular reflectance from diffraction is related to the sinusoidal height-field $h(x, y)$ through spectral diffraction BRDF given by [Stam 1999, Equation (7)] as

$$\mathfrak{f}_r^p(\omega_i = 0, \omega_r = 0) \propto |\mathfrak{F}\{p(x, y)\}(0, 0)|^2, \quad \text{where} \qquad (11)$$

$\mathfrak{F}$ is the Fourier transform of an auxiliary function: $p(x, y) = e^{i\frac{2\pi(\cos\theta_i + \cos\theta_r)}{\lambda}h(x,y)}$. ω_i and ω_r are solid angles representing incidence and view directions and θ_i,θ_r are angles between the surface normal and these directions respectively. For our specular imaging setup with near normal incidence, both tend to align with the surface normal: $\mathfrak{F}\{p\}(0, 0) = \int_{-\infty}^{-\infty}\int_{-\infty}^{-\infty} e^{i\frac{4\pi}{\lambda}h(x,y)}dxdy$. Now consider another grating with period $s = p/K$, and the corresponding transform $\mathfrak{F}\{p_2\}(0, 0) = \int_{-\infty}^{-\infty}\int_{-\infty}^{-\infty} e^{i\frac{4\pi}{\lambda}h(Kx,y)}dxdy$. Changing variable $x^* = Kx$ and simplifying this equation gives a simple relation $\mathfrak{F}\{p_2\}(0, 0) = \frac{1}{K}\mathfrak{F}\{p\}(0, 0)$. Since the constant of proportionality in Eq. 11 does not change with grating periodicity, we obtain the relation between corresponding BRDFs as $\mathfrak{f}_r^k(\omega_i = 0, \omega_r = 0) = \frac{1}{K^2}\mathfrak{f}_r^p(\omega_i = 0, \omega_r = 0)$. This relation is valid for both p- and s- polarizations[5] and $\mathbf{D}^s = \mathbf{D}^p/K$. Thus, specular intensities decrease proportionally with an inverse-squared law for the decrease in the grating periodicity parameter p[6], i.e. $I^p/I^s = K^2$ for respective specular intensities.

To compute relative periodicities, we first compute mean intensity I_{mean} for each pixel over all images taken with our setup. We then divide each I_{mean} by the maximum of all I_{mean} values. The normalized value represents relative $\frac{1}{K^2}$ terms. We then take the square roots to determine relative changes, i.e. $1/K$, with respect to the slowest grating dot or in other word, the grating dot with the longest periodicity p. At runtime, p can be chosen arbitrarily and relative periodicity of all other pixels can then be computed by scaling p with $1/K$. More generally, we re-target the range 0—1 for $1/K$ map to an arbitrary range $[p_{\min}, p_{\max}]$ for periodicities. Results with periodicity measurements are presented in Section 6.2.

[5]The BRDFs are linearly related to intensities where as Jones matrices are dealing with wave amplitudes. Since intensities have a square-law relation with the amplitude, the corresponding scale factor for $\mathbf{D}^s$ is the square-root of $\frac{1}{K}$

[6]Decrease in period p means more grating lines per mm.

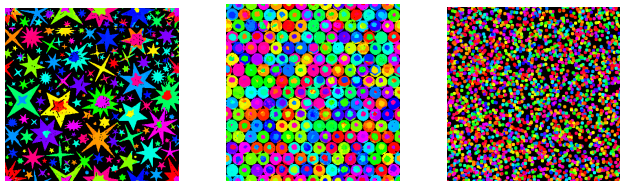

(a) (b) (c)

Fig. 17. Measured exemplar tiles with the flash illumination method. The orientations are encoded as the HSV color wheel mapped to the 0 to 180 degrees range. **(a)** Holographic gift bag with a star pattern. **(b)** Holographic gift bag with circles. **(c)** Stochastic holographic paper.

6 ADDITIONAL RESULTS

6.1 Flash illumination measurement

We present several orientation tiles acquired using the flash illumination setup in Fig. 17. Rendering comparison to photographs of these samples are presented in the accompanying supplemental document. The measured exemplar tile is repeated 12×8 times in order to create a full size holographic paper. The rendering is computed with a Gaussian point light source assuming a cool blue light spectrum (inverse of CIE illuminant A as employed by [Toisoul and Ghosh 2017a]) which looks visually similar to the spectrum of the smartphone flash. The spectral integration is computed in CIE XYZ space inside a fragment shader using the BRDF presented in Eq. 2, and with a wavelength sampling of 5 nanometers. Note that the runtime spectral integration allows to render holographic surfaces with varying periodicities.

6.2 Polarization imaging

Qualitative evaluations and adaptive bilateral filtering. Fig. 18 shows results for the holographic SIGGRAPH logo acquired using polarization imaging. The logo is about $15mm$ in diameter which makes it too small for the flash-illumination method. Our polarization imaging method solves for grating orientations with a very high accuracy of sinusoidal fitting. Note that the raw orientation map shown in Fig. 18b exhibits some low frequency variations due to local surface bumps on the sample during acquisition. These variations in the raw map lead to discontinuities in renderings (please see Fig. 8a—d, Row 2, in the supplemental material). We propose an adaptive and iterative bilateral filtering approach to clean measured orientation maps. This filtering is done in corresponding sine-cosine domain for orientation angles with arctan transformation for filtered results. We adapt bilateral filtering to take into account: (i) mask to disregard non-diffractive pixels while filtering, (ii) pixel-level error measure for the sinusoidal fit, and (iii) a local window to compute a median which is then used as the pivot value for bilateral filtering. Fig. 18c shows a map with few(ten) iterations of filtering that remove discontinuity artefacts for point-source renderings while retaining some realistic variations. Fig. 18e—h, second-row, show a few renderings under point-light with this orientation map. These renderings match subjectively well with reference photographs to light up corresponding polygons with diffraction colors. Note that color

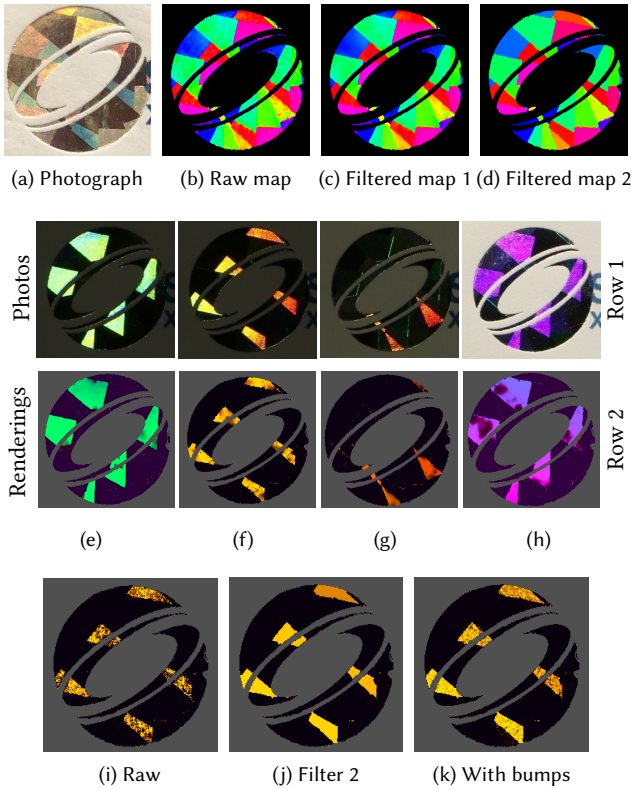

Fig. 18. Holographic SIGGRAPH Logo. Results generated with 12 images with polarizer filter rotation steps of about 13°. (a) Photograph in room-light. (b)–(d) Grating orientation maps estimated using polarized acquisition method. (b) Raw estimated map. (c) and (d) show two different levels of filtering using our adaptive bilateral filtering. (e)–(h) collectively show photographs under flash-light in the top-row. Row 2 shows renderings using filtered map 1 from (c) which show subjectively similar polygon patterns as above them. (i) and (j) show renderings similar to the photo in (f) while using maps from (b) and(d) respectively. (k) shows a similar rendering with map (d) plus synthesized surface bumps.

Fig. 19. Holographic emblem on a currency note. Results generated with 17 images at polarizer filter rotation steps of about 13°. (a) Photographic image under a mobile torch-light illumination is subjective matched by our rendering with fine geometric details in (e). (b) Room-light illumination reveals colorful bands across the emblem. (c) Gradient orientation map from our CPI method also shows such bands in false colors. (d) Periodicity variations are depicted in grayscale where white represents the longest period (lowest line count per mm).

Fig. 20. Orientation maps for tiles with continuously varying orientations. (a) Gradient stars. (b) Fireworks tile. Left map is estimated using polarization imaging. Right map is using flash-illumination. Fine details are retrievable with polarization imaging.

tones differ slightly in our renderings as we do not model white-light reflections from back-paper upon full transmission through semi-transparent logo. We also filter the raw map heavily (with 50 iterations) to have only sharp variations in the map (see Fig. 18d). Such a map is better suited for rendering with environment maps as shown in Fig. 1c where polygons have low but continuous color variations. Under torch-light, heavy filtering may introduce minor bias and slight subjective deviations. For eg., in Fig. 8c (Row 4) in the supplemental material, the orange triangle on the left is not simultaneously light under similar lighting conditions as for two rows above. However, with slight deviation in the lighting conditions this triangle reappears (not shown). Finally, Fig. 18k shows our rendering with a surface bump-map and the filtered orientation map from Fig. 18d. Here, we employed the bump map of a holographic paper acquired with step-edge illumination [Wang et al. 2011]. Fig. 18i with raw map shows black regions with missing diffraction inside yellow-orange polygons. These missing diffraction effects are recovered well through heavy filtering (see Fig. 18j) and Fig. 18k shows that adding surface bumps make renderings look more realistic.

Next, we present results with both grating orientation as well as periodicity maps. Fig. 19 shows the rendering of holographic emblem on a Ten pound currency note. This example has many fine scale features that are well presented in our maps as well as renderings. Fig. 19c shows near horizontal bands of different orientations at the top of the emblem. They are consistent in geometric layout with colorful bands observed in a reference photograph under room-lighting (Fig. 19b). Non-diffractive pixels are represented in black color and marked using an intensity threshold. Fig. 19d shows the periodicity map with fine concentric rings of high period lengths. These rings result in subtle diffraction effects, similar to those observed in images. Finally, Fig. 19e shows a rendering with these maps under a point-light with the crown lit in green similar to the photograph. The rendered colors differ slightly in the rendering as we do not match the spectral profile for the flash light and the absolute periodicities of the real grating dots remain unknown. We also resolved two more sample tiles with continuous orientation variations. One has diffractive stars of different sizes while the second one has firework like pattern of strokes, circles and small stars. Figure 20 shows resultant orientation maps obtained using the polarization setup. We present renderings for these cases in Section 6 for the supplemental material. The example with firework pattern is particularly difficult to solve with our flash-illumination method due to its fine-detail features.

6.3 Environmental rendering

We present environmental rendering of various acquired holographic papers in Fig. 21 using the rendering method of [Toisoul and Ghosh 2017b]. Note that for performance reasons, we do not take into account the Gaussian coherence window in the environmental rendering and only use a delta Dirac response instead. Note that such an approximation does not affect the rendering result much as the convolution with the environment already blurs the diffraction pattern. We also used a wavelength sampling of 20 nanometers for the spectral integration of the BRDF in order to increase the framerate without noticing any color artifact in the diffraction pattern. At full HD resolution, we achieved a framerate of 30 FPS with an NVIDIA 1080 GPU.

6.4 Artistic design

Having access to such orientation and periodicity maps enables creation of new types of effects such as the one shown in Fig. 22. The original gift bag with circles has a constant periodicity over the entire bag, hence producing a circularly shaped diffraction. Here, we apply a varying periodicity on each feature of the bag. Such an effect was produced by dividing the orientations of the circles in 180 bins, and giving a quadratic blend (Fig. 22a) or a sinusoidal blend (Fig. 22b) between a minimum periodicity (corresponding to 0° orientation) and a maximum (corresponding to 179° orientation). We provide the dataset of measured maps to the community.

7 EVALUATION AND DISCUSSION

7.1 Periodicity measurement from simulated data

We first evaluate the periodicity measurement using flash illumination as described in Section 4.4. As we do not have access to the true periodicity of our samples, we employ simulated data generated by our renderer. We rendered a holographic paper (here the polygonal pattern) at single wavelength ($\lambda = 560\ nm$) with a periodicity of 1.66 micrometers (600 lines per millimeter) under a Gaussian light source to take into account the fact that our flashlight is not a strict point light (Figure 23a). We save the corresponding non-normalized half-vector (Figure 23b). As explained in Section 4.4, under the sinusoidal grating assumption, the first order of diffraction appears at $|u| = \frac{\lambda}{a}$ where u is the projection of the non-normalized half-vector on the grating orientation. Using our simulated data, we found a periodicity that varies between 1.618 and 2.326 micrometers with an average of 1.939 μm and a standard deviation of $0.15\mu m$. The slight inaccuracy in the measurement is due to both the Gaussian coherence window that yields a Gaussian response to a diffracted wavelength instead of a delta Dirac (more details the supplemental material), as well as the Gaussian spread of light. However, this demonstrates that the periodicity of a sinusoidal grating can be measured accurately enough to be able to reproduce the subjective effects in rendering.

7.2 Manual selection of tiles

In this section we evaluate the manual selection of the tiles in the flash illumination method and look at the consequences of slight misalignments between the tiles on the recovered orientations. We manually selected a single reference tile (Figure 24a) and automatically inferred all the other tiles on the holographic paper by assuming that their position are given by a translation of the reference tile. Such a process leads to a misalignment of the tiles with regards to the reference tile (Figure 24b). We then compute our algorithm using the set of misaligned tile and recover the master orientation tile shown in Figure 24c. As expected the misalignments produce errors in the recovered orientations especially at the edges of the polygons compared to the reference solution shown in Figure 8.

7.3 Orientation measurement of a CD disk

We now present quantitative evaluation for the polarization imaging method. We solved for the grating orientations on an unwritten SONY CD, which has a known arrangement of diffractive tracks. The tracks spiral out with grating orientations being tangential to local radial vectors for the disc. Fig. 25a shows the orientation map for a central region of the disk, $100mm$ in diameter. For error estimation, we need to first compute and deduct the global offset $\psi_{\text{g\_off}}$. Fig. 25b shows the reference map which is used for comparison to compute $\psi_{\text{g\_off}}$ and Fig. 25c shows the estimated grating orientation map after accounting for $\psi_{\text{g\_off}}$. This aligned orientation map has a mean error of $\mu_{\text{error}} = 3.616^\circ$ and standard deviation $\sigma_{\text{error}} = 3.016^\circ$ in the estimates. These error estimates are affected by the inner ring that has some text prints and systematic deviations. The sample size here is also rather large and we deviate from near-normal conditions near the edges. Finally, the actual signal encoding the sinusoid has a much lower amplitude in comparison to the mean intensities in the diffractive region. We might be able to achieve lower errors using HDR imaging.

We also quantify sinusoid fitting errors in solving grating orientations for two samples. We measure these errors with normalized correlation factors between the fitted sinusoid and the $\widehat{I}_{norm}$ data for each grating dot/pixel in the tile. With value 1 indicating a perfect fit, we found mean correlation error factors for the kinematic and SIGGRAPH logo tiles to be 0.942 and 0.984 respectively.

8 LIMITATIONS AND METHOD COMPARISON

Both of our measurement approaches have advantages and disadvantages. Both usually employ a small number of photographs: one to five for flash illumination, and a minimum of four photographs for polarization imaging. The flash illumination method has the advantage of being very simple and accessible without the requirement of any additional optical components. It works better for holographic surfaces with discrete orientations, creates a discretization of continuously varying tiles and leads to measurements at a lower spatial resolution due to requiring to observe a larger sample area. Besides, it works under the assumption of tileable surfaces and cannot recover orientations on small holographic patterns. However, it can resolve stochastic holographic surfaces as well as measure absolute periodicities assuming that the camera is calibrated. The polarization imaging method has complementary strengths and weaknesses. It can resolve non-repetitive holographic patterns with fine features and continuous variations of orientation. However, it is limited to samples of smaller size (upto 7×7 cm^2) due to reliance on near normal incidence imaging with LCD illumination. This method generally works well with 6 to 12 images. However, it may require

(a) (b) (c) (d)

Fig. 21. Environmental renderings. **(a)** Circles holographic paper in bar environment acquired with the flash illumination method. **(b)** Kinematic pattern in kitchen environment acquired with the polarized imaging setup. **(b)** Hologram on a ten pound bank note in bar environment acquired with the polarized imaging setup. **(c)** Holographic paper with gradient variations inside the stars in bar environment measured with the polarized imaging setup.

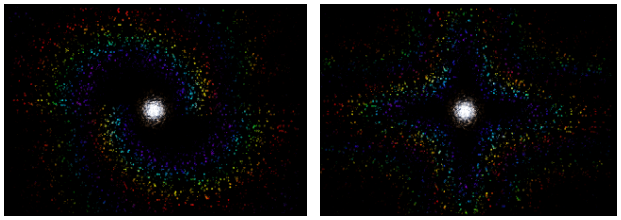

(a) (b)

Fig. 22. Creating new artistic effects using the measured maps by varying the periodicities. Periodicity variation following a square curve **(a)** and a sine squared curve **(b)**.

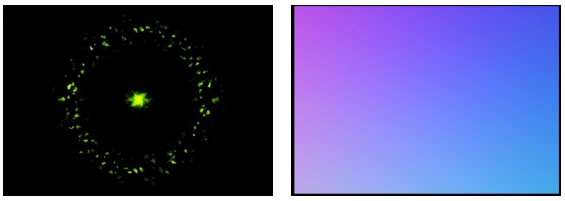

(a) (b)

Fig. 23. Computing the periodicity of the diffraction grating from a green spectral measurement **(a)** with known half vector directions encoded as XYZ=RGB **(b)**. The data was generated with a renderer, using 600 lines per millimeter for the diffraction grating and $\lambda = 560nm$.

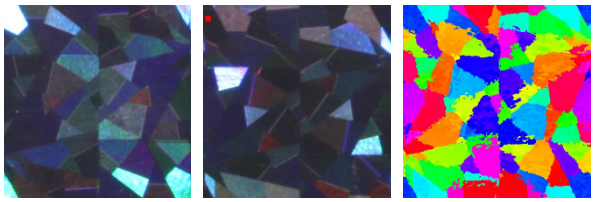

(a) (b) (c)

Fig. 24. Computation of the orientation tile with slight misalignment between the tiles. **(a)** Reference manually selected tile. **(b)** One of the misaligned tiles. The red square shows the top left corner of the reference tile **(c)** Recovered orientation map with misalignments between the tiles. A higher error is visible in the orientations especially at the border between two polygons compared to that shown in Fig. 8.

a larger number of measurements for some samples (up to 17 in our experiments) due to low SNR of the signal for sinusoidal fitting

(a) Raw map (b) Reference map (c) Re-aligned map

Fig. 25. Quantitative evaluations for polarization method using an unwritten CD disk. The region used for evaluations is about 100mm in diameter. (a) The raw orientation map estimated by our method. (b) The corresponding reference orientation map. (c) The raw map rotated to aligned with the reference map. For the estimates: $\mu_{\text{error}} = 3.616^\circ$ and $\sigma_{\text{error}} = 3.016^\circ$.

compared to the mean intensity, and can only recover relative periodicities and orientations. In summary, while the polarization imaging approach is indeed more general, it is also more complicated from the perspective of measurement and solving the inverse problem. This is why we employ the simpler flash illumination setup for repetitive samples which can be resolved well with a few measurements using flash illumination. The two methods also share a common limitation: currently none of them can solve for orientations and periodicities in multi-layered holographic surfaces.

9 CONCLUSION

We have presented two novel and complementary approaches for acquiring spatially varying diffraction due to 1-D sinusoidal gratings in commonly manufactured holographic surfaces. Such spatially varying surfaces are increasingly common in our daily lives, generate striking and beautiful iridescence, and have not been previously acquired for computer graphics applications. Our first setup simply involves a set of photographs under spectrally filtered flash illumination and can resolve the appearance of many interesting repeating and stochastic holographic samples. Our second setup using polarization imaging is a bit more involved, requiring an LCD panel and various optical accessories. However, the method can resolve complex non-repetitive holographic patterns with fine features. We present real-time photorealistic renderings of many common holographic surfaces and patterns using the two proposed acquisition setups. Given the fine scale imaging, the proposed polarization imaging approach could also be employed for inspection and defect detection in manufactured holographic samples. We further demonstrate generation of novel diffraction patterns using artistic

editing operations on the acquired orientation and periodicity maps, and we make all our acquired maps available to the community.

ACKNOWLEDGMENTS

This work was supported by an EPSRC Early Career Fellowship EP/N006259/1, a Royal Society Wolfson Research Merit Award, an SNSF Early Postdoc.Mobility Fellowship P2BEP2_165343, and the EPSRC Centre for Doctoral Training in High Performance Embedded and Distributed Systems (HiPEDS, grant EP/L016796/1). We also thank NVIDIA Corporation for providing a Titan Xp graphics card and Mirri who provided us with holographic papers. We thank the Bank of England for permissions for the banknote hologram example.

REFERENCES

Emmanuel Agu and Francis S. Hill Jr. 2002. Diffraction Shading Models For Iridescent Surfaces. In *Proc. IASTED VIIP.*

Miika Aittala, Tim Weyrich, and Jaakko Lehtinen. 2015. Two-shot SVBRDF Capture for Stationary Materials. *ACM Trans. Graph.* 34, 4, Article 110 (July 2015), 13 pages. https://doi.org/10.1145/2766967

Laurent Belcour and Pascal Barla. 2017. A Practical Extension to Microfacet Theory for the Modeling of Varying Iridescence. *ACM Trans. Graph.* 36, 4, Article 65 (July 2017), 14 pages. https://doi.org/10.1145/3072959.3073620

Kai Berger, Andrea Weidlich, Alexander Wilkie, and Marcus Magnor. 2012. Modeling and Verifying the Polarizing Reflectance of Real-World Metallic Surfaces. *IEEE Computer Graphics and Applications* 32, 2 (March 2012), 24–33.

R. L. Cook and K. E. Torrance. 1982. A Reflectance Model for Computer Graphics. *ACM Trans. Graph.* 1, 1 (Jan. 1982), 7–24. https://doi.org/10.1145/357290.357293

Tom Cuypers, Tom Haber, Philippe Bekaert, Se Baek Oh, and Ramesh Raskar. 2012. Reflectance Model for Diffraction. *ACM Trans. Graph.* 31, 5, Article 122 (Sept. 2012), 11 pages. https://doi.org/10.1145/2231816.2231820

Paul E. Debevec and Jitendra Malik. 1997. Recovering High Dynamic Range Radiance Maps from Photographs. In *Proceedings of the 24th Annual Conference on Computer Graphics and Interactive Techniques (SIGGRAPH '97)*. ACM Press/Addison-Wesley Publishing Co., New York, NY, USA, 369–378. https://doi.org/10.1145/258734.258884

D.S. Dhillon, J. Teyssier, M. Single, I. Gaponenko, M.C. Milinkovitch, and M. Zwicker. 2014. Interactive Diffraction from Biological Nanostructures. *Comput. Graph. Forum* 33, 8 (Dec. 2014), 177–188. https://doi.org/10.1111/cgf.12425

Daljit Singh J. Dhillon and Abhijeet Ghosh. 2016. Efficient Surface Diffraction Renderings with Chebyshev Approximations. In *SIGGRAPH ASIA 2016 Technical Briefs (SA '16)*. ACM, New York, NY, USA, Article 7, 4 pages. https://doi.org/10.1145/3005358.3005376

Zhao Dong, Bruce Walter, Steve Marschner, and Donald P. Greenberg. 2015. Predicting Appearance from Measured Microgeometry of Metal Surfaces. *ACM Trans. Graph.* 35, 1, Article 9 (Dec. 2015), 13 pages. https://doi.org/10.1145/2815618

Abhijeet Ghosh, Tongbo Chen, Pieter Peers, Cyrus A. Wilson, and Paul Debevec. 2010. Circularly Polarized Spherical Illumination Reflectometry. *ACM Trans. Graph.* 29, 6, Article 162 (Dec. 2010), 12 pages. https://doi.org/10.1145/1882261.1866163

Xavier Granier and Wolfgang Heidrich. 2003. A Simple Layered RGB BRDF Model. *Graph. Models* 65, 4 (July 2003), 171–184. https://doi.org/10.1016/S1524-0703(03)00042-0

Xiao D. He, Kenneth E. Torrance, François X. Sillion, and Donald P. Greenberg. 1991. A comprehensive physical model for light reflection. *SIGGRAPH Comput. Graph.* 25, 4 (1991), 175–186.

Nicolas Holzschuch and Romain Pacanowski. 2017. A Two-scale Microfacet Reflectance Model Combining Reflection and Diffraction. *ACM Trans. Graph.* 36, 4, Article 66 (July 2017), 12 pages. https://doi.org/10.1145/3072959.3073621

Matthias B. Hullin, Johannes Hanika, Boris Ajdin, Hans-Peter Seidel, Jan Kautz, and Hendrik P. A. Lensch. 2010. Acquisition and Analysis of Bispectral Bidirectional Reflectance and Reradiation Distribution Functions. *ACM Trans. Graph.* 29, 4, Article 97 (July 2010), 7 pages. https://doi.org/10.1145/1778765.1778834

Masataka Imura, Osamu Oshiro, Masahiko Saeki, Yoshitsugu Manabe, Kunihiro Chihara, and Yoshihiro Yasumuro. 2009. A Generic Real-time Rendering Approach for Structural Colors. In *Proceedings of the 16th ACM Symposium on Virtual Reality Software and Technology (VRST '09)*. ACM, New York, NY, USA, 95–102. https://doi.org/10.1145/1643928.1643952

Wenzel Jakob, Miloš Hašan, Ling-Qi Yan, Jason Lawrence, Ravi Ramamoorthi, and Steve Marschner. 2014. Discrete Stochastic Microfacet Models. *ACM Trans. Graph.* 33, 4, Article 115 (July 2014), 10 pages. https://doi.org/10.1145/2601097.2601186

Menglin Jiang, Shiwei Lin, Wenkai Jiang, and Nengqian Pan. 2014. Hot embossing holographic images in BOPP shrink films through large-area roll-to-roll nanoimprint lithography. *Applied Surface Science* 311 (2014), 101–106.

Young-Min Kang, Do-Hoon Lee, and Hwan-Gue Cho. 2015. Multipeak Anisotropic Microfacet Model for Iridescent Surfaces. *Multimedia Tools Appl.* 74, 16 (Aug. 2015), 6229–6242. https://doi.org/10.1007/s11042-014-2092-1

Anat Levin, Daniel Glasner, Ying Xiong, Frédo Durand, William Freeman, Wojciech Matusik, and Todd Zickler. 2013. Fabricating BRDFs at High Spatial Resolution Using Wave Optics. *ACM Trans. Graph.* 32, 4, Article 144 (July 2013), 14 pages. https://doi.org/10.1145/2461912.2461981

Clifford Lindsay and Emmanuel Agu. 2006. Physically-based Real-time Diffraction Using Spherical Harmonics. In *Proceedings of the Second International Conference on Advances in Visual Computing - Volume Part I (ISVC'06)*. Springer-Verlag, Berlin, Heidelberg, 505–517. https://doi.org/10.1007/11919476_51

Heylal Mashaal, Alex Goldstein, Daniel Feuermann, and Jeffrey M. Gordon. 2012. First direct measurement of the spatial coherence of sunlight. *Optics Letters* 37, 17 (2012), 3516–3518.

Wojciech Matusik, Hanspeter Pfister, Matt Brand, and Leonard McMillan. 2003. A Data-driven Reflectance Model. *ACM Trans. Graph.* 22, 3 (July 2003), 759–769.

Addy Ngan, Frédo Durand, and Wojciech Matusik. 2005. Experimental Analysis of BRDF Models. In *Rendering Techniques*. 117–226.

Jérémy Riviere, Ilya Reshetouski, Luka Filipi, and Abhijeet Ghosh. 2017. Polarization Imaging Reflectometry in the Wild. *ACM Trans. Graph.* 36, 6, Article 206 (Nov. 2017), 14 pages. https://doi.org/10.1145/3130800.3130894

William John Roff and John Richard Scott. 2013. *Fibres, films, plastics and rubbers: a handbook of common polymers*. Elsevier.

Jos Stam. 1999. Diffraction Shaders. In *Proceedings of the 26th Annual Conference on Computer Graphics and Interactive Techniques (SIGGRAPH '99)*. ACM Press/Addison-Wesley Publishing Co., New York, NY, USA, 101–110. https://doi.org/10.1145/311535.311546

Yinlong Sun. 2000. *A Spectrum-based Framework for Realistic Image Synthesis*. Ph.D. Dissertation. Advisor(s) Fracchia, F. David. AAINQ61686.

Yinlong Sun. 2006. Rendering Biological Iridescences with RGB-based Renderers. *ACM Trans. Graph.* 25, 1 (Jan. 2006), 100–129. https://doi.org/10.1145/1122501.1122506

Yinlong Sun, Mark S. Drew, and F. David Fracchia. 1999a. Representing Spectral Functions by a Composite Model of Smooth and Spiky Components for Efficient Full-Spectrum Photorealism. In *Proceedings of the 1999 IEEE Workshop on Photometric Modeling for Computer Vision and Graphics (PMCVG '99)*. IEEE Computer Society, Washington, DC, USA, 4–. http://dl.acm.org/citation.cfm?id=519626.826724

Yinlong Sun, F. David Fracchia, Thomas W. Calvert, and Mark S. Drew. 1999b. Deriving Spectra from Colors and Rendering Light Interference. *IEEE Comput. Graph. Appl.* 19, 4 (July 1999), 61–67. https://doi.org/10.1109/38.773965

Yinlong Sun, F. David Fracchia, Mark S. Drew, and Thomas W. Calvert. 2000. Rendering Iridescent Colors of Optical Disks. In *Proceedings of the Eurographics Workshop on Rendering Techniques 2000*. Springer-Verlag, London, UK, UK, 341–352. http://dl.acm.org/citation.cfm?id=647652.732138

Antoine Toisoul and Abhijeet Ghosh. 2017a. Practical Acquisition and Rendering of Diffraction Effects in Surface Reflectance. *ACM Trans. Graph.* 36, 5, Article 64c (July 2017). https://doi.org/10.1145/3012001

Antoine Toisoul and Abhijeet Ghosh. 2017b. Real-time Rendering of Realistic Surface Diffraction with Low Rank Factorisation. In *Proceedings of the 14th European Conference on Visual Media Production (CVMP 2017) (CVMP 2017)*. ACM, New York, NY, USA, Article 2, 7 pages. https://doi.org/10.1145/3150165.3150167

Borom Tunwattanapong, Graham Fyffe, Paul Graham, Jay Busch, Xueming Yu, Abhijeet Ghosh, and Paul Debevec. 2013. Acquiring Reflectance and Shape from Continuous Spherical Harmonic Illumination. *ACM Trans. Graph.* 32, 4, Article 109 (July 2013), 12 pages. https://doi.org/10.1145/2461912.2461944

Zdravko Velinov, Sebastian Werner, and Matthias B. Hullin. 2018. Real-Time Rendering of Wave-Optical Effects on Scratched Surfaces. to appear.

Chun-Po Wang, Noah Snavely, and Steve Marschner. 2011. Estimating Dual-scale Properties of Glossy Surfaces from Step-edge Lighting. *ACM Trans. Graph.* 30, 6, Article 172 (Dec. 2011), 12 pages. https://doi.org/10.1145/2070781.2024206

Gregory J. Ward. 1992. Measuring and Modeling Anisotropic Reflection. *SIGGRAPH Comput. Graph.* 26, 2 (July 1992), 265–272. https://doi.org/10.1145/142920.134078

Andrea Weidlich and Alexander Wilkie. 2008. Realistic Rendering of Birefringency in Uniaxial Crystals. *ACM Trans. Graph.* 27, 1, Article 6 (March 2008), 12 pages. https://doi.org/10.1145/1330511.1330517

Sebastian Werner, Zdravko Velinov, Wenzel Jakob, and Matthias B. Hullin. 2017. Scratch Iridescence: Wave-optical Rendering of Diffractive Surface Structure. *ACM Trans. Graph.* 36, 6, Article 207 (Nov. 2017), 14 pages. https://doi.org/10.1145/3130800.3130840

Ling-Qi Yan, Miloš Hašan, Bruce Walter, Steve Marschner, and Ravi Ramamoorthi. 2018. Rendering Specular Microgeometry with Wave Optics. *ACM Transactions on Graphics (Proc. SIGGRAPH)* 37, 4 (2018).

Genzhi Ye, Sundeep Jolly, V. Micheal Bove, Qionghai Dai, Ramesh Raskar, and Gordon Wetzstein. 2014. Toward BxDF Display using Multilayer Diffraction. *ACM Trans. Graph. (SIGGRAPH Asia)* 33, 6 (2014).